Research Square

Preprints are preliminary reports that have not undergone peer review.
They should not be considered conclusive, used to inform clinical practice,
or referenced by the media as validated information.

4α,5α-epoxy-10α,14H-1-epi-inuviscolide induces mitochondrial-mediated apoptosis and suppresses SW480 colorectal cancer cell growth in vitro and in vivo

Bikram Singh
CSIR-Indian Institute of Integrative Medicine
Shivani Rana
CSIR-Indian Institute of Integrative Medicine
Komal .
CSIR-Indian Institute of Integrative Medicine
Zabeer Ahmed
CSIR-Indian Institute of Integrative Medicine
Yedukondalu Nalli
CSIR-Indian Institute of Integrative Medicine
Boobalan Gopu
boobalang.iiim@csir.res.in
CSIR-Indian Institute of Integrative Medicine

Research Article

Keywords: Sesquiterpene lactone, Inuviscolide, Colorectal cancer, Apoptosis, Xenograft, Antitumor

Posted Date: November 12th, 2026

DOI: https://doi.org/10.21203/rs.3.rs-11508328/v1

License: This work is licensed under a Creative Commons Attribution 4.0 International License.
Read Full License

Additional Declarations: No competing interests reported.

4α,5α-epoxy-10α,14H-1-epi-inuviscolide induces mitochondrial-mediated apoptosis and suppresses SW480 colorectal cancer cell growth *in vitro* and *in vivo*

Bikram Singh[1, 3#] • Shivani Rana[1, 3#] • Komal[2, 3] • Zabeer Ahmed[1, 3] • Yedukondalu Nalli[2, 3] • Boobalan Gopu[1, 3*]

[1]Pharmacology Division, CSIR-Indian Institute of Integrative Medicine, Canal Road, Jammu - 180001, INDIA

[2]Natural Products and Medicinal Chemistry Division, CSIR-Indian Institute of Integrative Medicine, Canal Road, Jammu - 180001, INDIA

[3]Academy of Scientific and Innovative Research (AcSIR), Ghaziabad - 201002, INDIA.

[#]Contributed equally

[*]**Corresponding Author:** Boobalan Gopu: boobalang.iiim@csir.res.in

Summary

4*α*,5*α*-epoxy-10*α*,14H-1-epi-inuviscolide (INV), a guaianolide sesquiterpene lactone, has received limited pharmacological investigation beyond its reported antifungal and antibacterial activities; its anticancer effects remain entirely uncharacterized. Cytotoxicity, cellular and nuclear morphology, and clonogenic potential of INV were evaluated. Network pharmacology and Venn analysis cross-referencing INV's targets with SW480 transcriptomic data (GEO: GSE345612) identified five core apoptotic targets (*BAX*, *BCL2*, *CASP3*, *CASP9*, and *CYCS*). Binding of INV to the predicted pockets of BAX and BCL2 was evaluated using molecular docking. Apoptosis, cell-cycle distribution, and key associated regulatory proteins were assessed by flow cytometry and Western blotting. *In vivo* antitumor efficacy at 40 and 80 mg/kg (MPK) was evaluated in a SW480 tumour-bearing mouse model. Preliminary safety was assessed using a single acute oral toxicity study (OECD 423; 300 and 2000 MPK). INV exhibited antiproliferative activity across a panel of CRC cell lines, with the best activity against SW480 cells (IC_{50}: 4.65 μM). INV upregulated BAX, cleaved caspase 3, and cleaved PARP, and downregulated BCL2 and cell-cycle regulatory proteins, cyclin D1 and CDK4. Elevated reactive oxygen species (ROS) disrupted mitochondrial membrane potential and triggered cytochrome C release, implicating the intrinsic mitochondrial apoptotic pathway. Orally administered INV demonstrated significant tumour growth inhibition of 78.26% and 96.71% at 40 and 80 MPK, respectively. Acute toxicity evaluation at 300 and 2000 MPK revealed no clinical signs or mortality, indicating an LD_{50} > 5000 MPK. Collectively, these findings provide new evidence of INV efficacy in SW480 cells, supporting further investigation of INV as a potential anticancer lead.

Keywords Sesquiterpene lactone • Inuviscolide • Colorectal cancer • Apoptosis • Xenograft • Antitumor

Introduction

Colorectal cancer (CRC) is the third most commonly diagnosed cancer globally, accounting for approximately 1.9 million new cases and 0.9 million deaths annually [1, 2]. Although incidence rates have declined among older adults in high-income countries, a significant rise has been observed among younger individuals (< 50 years) [3]. Treatment of advanced and metastatic CRC relies on fluoropyrimidine-based regimens (5-FU/capecitabine) combined with oxaliplatin or irinotecan and targeted agents such as anti-VEGF and anti-EGFR antibodies; however, intrinsic or acquired drug resistance, tumour heterogeneity, and systemic toxicity substantially limit their long-term efficacy and safety [4]. Although immunotherapy has shown benefit in patients with deficient mismatch repair, most CRC cases are mismatch repair proficient and respond poorly. These limitations underscore the need for mechanistically novel anticancer agents with improved therapeutic windows.

Natural products and their semi-synthetic derivatives remain a rich source of anticancer leads, with sesquiterpene lactones (STLS), particularly guaianolides, attracting particular interest owing to their α-methylene-γ-lactone (AMGL) pharmacophore. AMGL moiety covalently modifies cysteine thiols in key oncogenic proteins to suppress tumour proliferation, induce apoptosis, and overcome multidrug resistance [5]. Our group is interested in identifying bioactive natural products, including guaianolides with potent anticancer activity, from the Himalayan flora [6, 7]. In continuation of our efforts, we isolated 4α,5α-epoxy-10α,14H-1-epi-inuviscolide (INV), a guaianolide from the aerial parts of *Inula racemosa* Hook.f., a member of the *Asteraceae* family [8, 9]. INV was first isolated from *Carpesium abrotanoides* (Syn. Pig's head; *Asteraceae* family), a plant native to the Himalayan regions [10, 11]. INV possesses the characteristic STL skeleton and AMGL moiety, together with an epoxide ring between C4 and C5 and a C10-C14 exocyclic double bond reduced to a single bond, conferring distinct chemical reactivity and biological properties. Published reports on INV are limited to antifungal and antibacterial activities [12]. However, its stereoisomer, 4α,5α-epoxy-10α,14-dihydro-inuviscolide, has demonstrated suppression of nuclear factor kappa B (NF-κB)-driven pro-inflammatory cytokine production in acute inflammatory conditions [11] and cytotoxicity against cancer cell lines (< 5 μM) [10]. The former shares a core scaffold, an epoxy bridge, and a reduced exocyclic group with the latter, but differs stereochemically (inverted; epimeric at C1) compared to the natural configuration of the latter dihydro variant, resulting in distinct biological activity profiles.

Despite this pharmacological precedent, no study has systematically investigated cytotoxicity, apoptotic mechanism, cell cycle effects, or *in vivo* antitumor activity of INV against CRC. The present study addresses this gap by providing an integrated mechanistic evaluation of INV in SW480 colon adenocarcinoma cells, incorporating *in silico*, *in vitro,* and *in vivo* approaches.

Materials and methods

Chemistry

INV was used from our previous study [8, 9].

Cell lines and growth conditions

A panel of human cancer cell lines was obtained from three established cell repositories: the National Centre for Cell Science (NCCS, Pune, India), the National Cancer Institute (NCI, Bethesda, Maryland, USA), and the European Collection of Authenticated Cell Cultures (ECACC, Salisbury, UK). Detailed information, including catalogue numbers, mycoplasma testing, and STR profiling authentication, is summarised in Table S5. Cell lines were maintained in RPMI-1640 or DMEM culture medium (ThermoFisher Scientific–Gibco, Grand Island, New York, USA) supplemented with 10% fetal bovine serum (FBS; Gibco), penicillin/streptomycin (Gibco),4-(2-hydroxyethyl)-1-piperazineethanesulfonic acid) (HEPES; Sigma-Aldrich, St. Louis, Missouri, USA), and sodium bicarbonate (ANJ Biomedicals LLC, Bordentown, New Jersey, USA). Cells were incubated in an ESCO incubator (CCL-170T-8-UV-WJ) at 37 °C, 95% humidity, and 5% CO_2. Detailed information about the chemicals, reagents, plasticware, and glasswares used is provided in Tables S2-S3.

In vitro formulation

Primary 10mM stock solutions of INV and 5-FU were prepared in dimethyl sulfoxide (DMSO; SRL Chemicals, Mumbai, India) and diluted with culture medium to obtain the working concentrations, with final DMSO below 0.16% (*v/v*) and 0.08% (*v/v*) for SRB and mechanistic studies, respectively. Vehicle control groups were treated with < 0.1% (*v/v*) DMSO, which exhibited no observable effect on cell viability or cellular phenotype.

Sulforhodamine B (SRB) cytotoxicity assay

Briefly, cells were seeded into 96-well flat-bottom plates and treated with INV (0.5-16 μM) or the reference control, 5-fluorouracil (Cayman Chemicals, Ann Arbor, USA) for 48 h. Following treatment, the cells were fixed with chilled 50% (*w/v*) trichloroacetic acid (TCA; Himedia, Thane, India; 1 h, 4 °C). Plates were subsequently washed with water and allowed to air-dry overnight. Fixed cells were stained with 0.4% (*w/v*) SRB (Thermo Fisher Scientific, Waltham, Massachusetts, USA) in 1% (*v/v*) acetic acid (Thermo Fisher Scientific, USA) for 1 h at room temperature (RT). Excess unbound dye was removed with 1% (*v/v*) glacial acetic acid (Thermo Fisher Scientific) followed by overnight air-drying. The dye retained by cellular proteins was subsequently solubilised in 100 μL of 10 mM Tris-base (Sigma-Aldrich), and absorbance (optical density, OD) was measured at 540 nm using a Tecan™ Infinite® M-Plex multimode microplate reader. Cell viability (%) was calculated relative to untreated controls using the formula: OD-treated/OD-control) × 100 [7].

Colony formation assay

SW480 cells (500-1000 cells/well) were seeded in 6-well plates and allowed to attach overnight. Cells were treated with INV or 5-FU for 48 h. Following treatment, media were removed, plates were washed with phosphate-buffered saline (PBS; Gibco), and fresh medium was added. Cells were maintained for 14 days, with medium replaced every 2-

3 days. Finally, cells were washed with PBS, fixed with 4% (*v/v*) paraformaldehyde (Himedia, India; 20 min, RT), and stained with 0.5% (*v/v*) crystal violet (Merck, USA; 20 min). Excess stain was removed by washing with distilled water, and the plates were air-dried [13]. Colonies were counted using ImageJ. Colony-forming ability was expressed as Colony formation (%) = Colonies in treated group/Colonies in control group × 100

Cell migration (Scratch) assay

Cells were seeded in 6-well plates and allowed to form a confluent monolayer. A sterile pipette tip was used to create a uniform linear scratch across the cell monolayer. Wells were gently washed with PBS to remove detached cells and treated with INV or 5-FU. Images of the scratched areas were captured at 0 h and 48 h using a bright-field microscope. The wound area was quantified using ImageJ, and wound closure was calculated as the percentage reduction in scratch area relative to 0 h [14].

Integrated computational workflow: from in silico target discovery to microenvironment transcriptomic mining

To determine the pharmacological profile of INV against CRC, an integrated computational workflow combined reverse pharmacology, transcriptomic mining, and network systems biology. The chemical structure of INV was submitted to the Swiss Target Prediction web server (https://www.swisstargetprediction.ch/) to identify potential human targets based on structural similarity metrics. The top-ranked hits (106 targets) were imported into the STRING database (v12.0; https://string-db.org/cgi/about) using a minimum interaction score of 0.700 to construct a baseline high-confidence Protein-Protein Interaction (PPI) network [15, 16]. To map these targets against a disease-relevant microenvironment, high-throughput RNA-sequencing data were retrieved from the NCBI Gene Expression Omnibus (GEO) under accession GSE345612. This dataset profiles transcriptomic shifts in human SW480 cells as they transition from two-dimensional (2D) monolayer culture to three-dimensional (3D) tumour spheroids [https://www.ncbi.nlm.nih.gov/gds/?term=SW480+colorectal+cancer]. Differentially expressed genes (DEGs) were identified using a nominal statistical threshold of $p < 0.05$ [17].

A Venn diagram of the intersection between the 106 predicted INV targets and the 5,403 nominally significant DEGs from GSE345612 was generated using an online Venn tool [18]. This intersection identified a consensus set of five apoptosis-associated target genes: *BAX*, *BCL2*, *CASP3*, *CASP9*, and *CYCS* (Cytochrome c). Target nodes were subsequently mapped to the Kyoto Encyclopedia of Genes and Genomes (KEGG) database using the STRING engine, with a Benjamini-Hochberg false discovery rate (FDR) correction applied (FDR < 0.05). Enrichment results and differential expression matrices were visualised in Python (v. 3.13) using Seaborn (v. 0.13) and Matplotlib (v. 3.9). Prognostic survival analysis for *BAX*, *BCL2*, *CASP3*, and CYCS was performed using the GEPIA3 web server (https://gepia3.bioinfoliu.com) with recomputed RNA-sequencing data from The Cancer Genome Atlas (TCGA; COAD/READ cohorts). Survival risk profiles were visualised as a forest plot.

Molecular docking analysis

To characterise the potential intermolecular interactions of INV with the core regulators of mitochondrial apoptosis, molecular docking simulations were performed with human BCL2 (PDB ID: 1G5M) and BAX (PDB ID: 8SPZ).

High-resolution crystal structures were retrieved from the RCSB Protein Data Bank. Receptor preparation involved the removal of co-crystallised water molecules and non-protein entities, followed by conversion to the PDBQT format for use with AutoDock Vina (v. 1.2.7). INV was prepared in AutoDockTools with Gasteiger charges assigned and all rotatable bonds set to full torsional flexibility.

Target binding sites were identified using the PrankWeb web server, which implements the P2Rank machine learning algorithm (https://prankweb.cz/). Pocket 1, which yielded the highest ligand ability score for both targets, was selected for docking. Grid box centres were locked onto the exact coordinates derived from the PrankWeb surface calculations: BCL2: X, Y, Z = -0.8520, 5.1431, 10.6928; BAX: X, Y, Z = 10.8058, -10.6489, 26.8159. A uniform cubic search volume of 40 × 40 × 40 grid points with a grid spacing of 0.357 Å (15 × 15 × 15 Å) was applied to both targets. Exhaustiveness was set to 8, generating a maximum of 9 binding modes within a 3 kcal/mol energy window. The lowest-energy binding conformation (mode 1) was selected for analysis. 3D binding orientations within the target binding pockets were evaluated using PyMOL, and 2D interaction maps were generated using BIOVIA Discovery Studio Visualizer.

Scanning electron microscopy (SEM)

Cells were seeded onto sterile glass coverslips placed in 6-well plates and treated with INV or 5-FU for 48 h. Following treatment, cells were rinsed with PBS and fixed with 5% (*v/v*) glutaraldehyde (Sigma-Aldrich; 4 °C, overnight) to preserve their cellular architecture and surface morphology. After fixation, cells were washed to remove excess fixative and post-fixed with 1% (*v/v*) osmium tetroxide (OsO_4; Tokyo Chemical Industry, Tokyo, Japan; 1 h, dark, RT). Samples were washed with distilled water and dehydrated using a graded ethanol series ranging from 70% to 100% (*v/v*) (Fine Chemicals, Changshu, China) for 10 min at each step. Coverslips were dried, mounted, and sputter-coated with a thin gold layer to enhance electrical conductivity and image resolution. Samples were examined using an EOL JSM-IT300 to evaluate treatment-associated alterations in cell surface morphology [19].

Fluorescent Imaging Assays (DAPI, ROS, MMP and AO/EtBr staining)

Changes in nuclear morphology, intracellular ROS levels, and mitochondrial membrane potential ($\Delta\Psi M$) were examined using the fluorescent probes DAPI (4',6-diamidino-2-phenylindole), DCFH-DA (2',7'-dichlorodihydrofluorescein diacetate), and rhodamine-123, respectively. 5-FU (20 μM) and 0.05% (*v/v*) H_2O_2 (Central Drug House, New Delhi, India) were used as positive controls (PC). For nuclear morphology, SW480 cells were seeded (2×10^5 cells/well) in 6-well plates and exposed to INV or 5-FU for 48 h. Cells were washed with phosphate-buffered saline (PBS), fixed with ice-cold 4% (*v/v*) paraformaldehyde (Himedia; 20 min), washed with PBS, and incubated with DAPI (10 μg/mL; SRL Chemicals; dark, 30 min). Nuclear morphological alterations were examined using a fluorescence microscope (Thermo Fisher Scientific™ EVOS FLc) [20]. For $\Delta\Psi M$ assessment, treated cells were stained with 200 *n*M rhodamine-123 (Sigma-Aldrich) and incubated (20 min, 37°C, dark), washed with PBS, resuspended in serum-free media, and examined under a fluorescence microscope [21]. For intracellular ROS measurement, treated cells were incubated with 10 μM DCFH-DA (Sigma-Aldrich; 30 min, 37°C, dark), rinsed with PBS, and examined under a fluorescence microscope [22]. For acridine orange (AO) and ethidium bromide (EtBr) staining, treated SW480 cells were washed with PBS, stained with a freshly prepared 1:1 mixture of AO/EtBr, each at

100 μg/mL (Sigma-Aldrich; 5 min, RT, dark), and immediately examined using a fluorescence microscope to visualise and differentiate live, early apoptotic, late apoptotic, and necrotic cell populations based on their characteristic fluorescence patterns [23].

Annexin V-FITC/PI apoptosis assay

Following INV or 5-FU treatment, cells were collected, rinsed twice with PBS, resuspended in 1X Annexin-binding buffer, and incubated with Annexin V-FITC and propidium iodide (PI) using a commercially available apoptosis detection kit (ThermoFisher Scientific; 15 min, RT, dark). Apoptotic cell populations were quantified by flow cytometry using a BD Biosciences FACS Lyric™.

Western blotting

Following treatment, cells were rinsed with PBS, collected by centrifugation, and lysed in an ice-cold radioimmunoprecipitation assay (RIPA) buffer (Sigma-Aldrich) supplemented with 0.5 mM sodium orthovanadate (Na_3VO_4; Sigma-Aldrich), 2 mM phenylmethylsulfonyl fluoride (PMSF; Merck, Burlington, USA), 50 mM sodium fluoride (NaF; Sigma-Aldrich), and a protease inhibitor cocktail (Promega, Fitchburg, Wisconsin, USA). Lysates were incubated (45 min), then centrifuged (12,000 rpm, 20 min, 4 °C; Eppendorf 5830R). Protein concentration in the resulting supernatants was quantified by the Bradford assay. Equal amounts of protein were mixed with sodium dodecyl sulfate-polyacrylamide gel electrophoresis (SDS-PAGE) sample buffer (SRL Chemicals), resolved by SDS-PAGE (70 V, 3 h), and electrotransferred onto polyvinylidene fluoride (PVDF) membranes (Merck; 100 V, 2 h). Membranes were then blocked with 5% (*w/v*) bovine serum albumin (BSA; Himedia) in Tris-buffered saline containing 0.1% (*v/v*) Tween-20 (TBST; Sigma-Aldrich) for 1 h. Membranes were incubated (overnight, 4°C) with the respective primary antibodies, washed thrice with TBST (5 min/wash), and incubated with horseradish peroxidase (HRP)-conjugated secondary antibodies (1:1000; 1 h, RT) [24]. Protein bands were visualised using a luminol-based chemiluminescent substrate (Bio-Rad, Hercules, California, USA) on a ChemiDoc Imaging System (Bio-Rad). All antibodies were procured from Cell Signalling Technology, Danvers, Massachusetts, USA, and are provided in Table S4.

Cell cycle analysis

Treated cells were collected, rinsed with PBS, and fixed using 70% (*v/v*) ethanol (overnight, 37°C). Fixed cells were treated with RNase solution (0.1 mg/mL; SRL Chemicals; 90 min, 37°C), followed by staining with 50 μg/mL PI (Cayman Chemicals). DNA content was assessed by flow cytometry to determine the distribution of cells across cell cycle phases [25].

In vivo formulation

INV was prepared in 5% DMSO (SRL Chemicals, India), 5% Tween 80 (Merck Life Sciences, India), 40% PEG-200 (SD Fine Chemicals, Mumbai, India), and 50 % distilled water (Table S1 and Fig. S1). 5-FU was administered as a solution in normal saline.

Animals

Athymic nude (Fox1^{nu}) and Swiss albino mice were housed in individually ventilated cages (IVC; Techniplast, Italy) in a barrier facility at CSIR – Indian Institute of Integrative Medicine (CSIR-IIIM), Jammu, under the regulated environmental conditions: 23 ± 2 °C, 50-60% relative humidity, > 12- 15 air changes/h, and a 12-h light/dark cycle. Animals are provided with a standard laboratory rodent pellet diet and reverse osmosis (RO) water *ad libitum.* All experimental protocols (471/88/02/2026 and 510/89/7/2026), approved by the Institutional Animal Ethics Committee (IAEC), CSIR-IIIM, were performed in accordance with the applicable Committee for Control and Supervision of Experiments on Animals (CCSEA) guidelines (2018) and the Guide for the care and use of laboratory animals [26].

Xenograft study

Briefly, 5 × 10^6 SW480 cells with basement membrane matrix (Corning, Bedford, USA) at a 1:1 ratio were implanted subcutaneously into the right flank of female nude mice [27]. Animals were randomised at a tumour volume of 100-150 mm^3 using the Latin square method into four experimental groups and dosed accordingly for 21 days: G1: Vehicle control, G2: 5-fluorouracil (5-FU; 30 MPK, intraperitoneal, thrice/week), and INV-treated groups (40 and 80 MPK; once daily, oral) (Fig. 8A). Body weight and tumour volume were measured three times per week using an animal weighing balance (Sartorius, Germany) and a digital Vernier calliper (Mitutoyo, Japan), respectively. Tumour volume (TV) was estimated using the formula: TV = (length × breadth^2)/ 2. On day 22, the animals were euthanised *by* cervical dislocation under 3% isoflurane anaesthesia; tumours were excised, weighed, and photographed.

Acute toxicity study

A single oral dose (300 or 2000 MPK) of INV was administered to healthy adult fasted (4 h) female Swiss albino mice (n = 3) in accordance with OECD guideline 423 (Acute Toxic Class Method). Following dosing, animals were observed for clinical signs of toxicity and mortality at 30-min intervals during the first 4 h, and daily for 14 days. Body weights were recorded before administration and at weekly intervals. On day 15, animals were euthanised, and gross examination of external surfaces and internal organs was performed to identify any INV-associated toxic abnormalities.

Statistical analysis

Data are expressed as the mean ± standard deviation (SD) of at least three independent experiments (n = 3). IC_{50} values were calculated by non-linear regression analysis of logarithmically transformed concentration-growth inhibition data using GraphPad Prism 7.0 (GraphPad Software, San Diego, California, USA). Colony count, fluorescence intensity, and Western blot densitometry were quantified using ImageJ (ver. 1.54; National Institutes of Health, Bethesda, Maryland, USA). Flow cytometry data were analysed using FCS Express (ver. 7.24.24; De Novo Software, Pasadena, California, USA). Figures were prepared and compiled using Inkscape (ver. 1.4; Open source). Group differences were evaluated using the appropriate methods as described in the corresponding figure captions. A p-value < 0.05 was considered statistically significant.

Results

In vitro antiproliferative activity of INV

INV exhibited concentration-dependent antiproliferative activity against a panel of human CRC cell lines (SW620, HT-29, HCT-116, and SW480), with the best activity observed against SW480 cells (IC_{50} = 4.65 μM) (Fig. 1B and C). INV suppressed the long-term clonogenic capacity (colony number and size) of SW480 cells in a concentration-dependent manner (Fig. 2A and B). Significant reductions ($p < 0.0001$) were observed at all three concentrations of INV, comparable to 5-FU. In the scratch wound assay, progressive wound closure was observed in the control group. In contrast, INV-treated cells exhibited a concentration-dependent reduction in residual wound area ($p < 0.001$ at 4 and 8 μM), indicating suppression of SW480 cell migratory capacity (Fig. 2C and D).

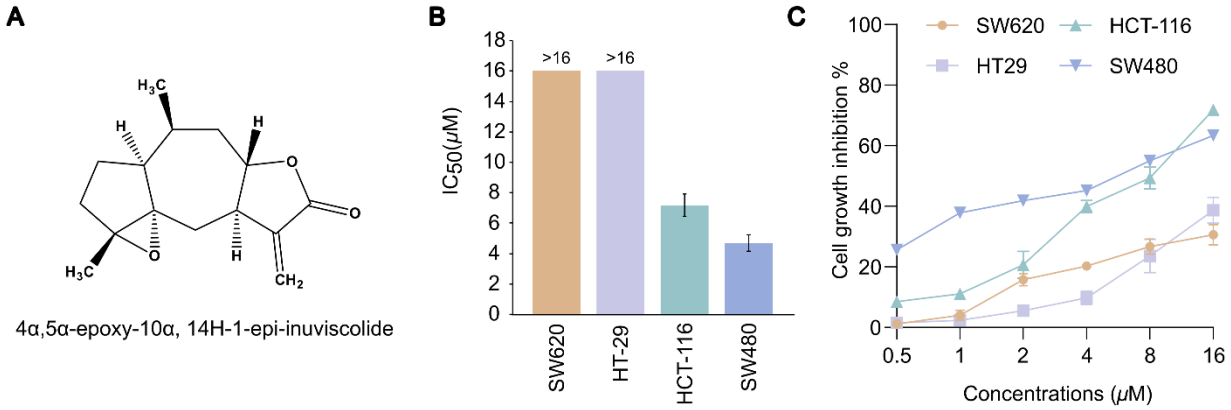


Fig. 1 Cytotoxicity of INV on a panel of human colorectal cancer cell lines. (A) Chemical structure of INV. (B) IC_{50} of INV against human CRC cancer cell lines. (C) Concentration-dependent cell growth inhibition (%) of INV against cell lines at 0.5-16 μM.

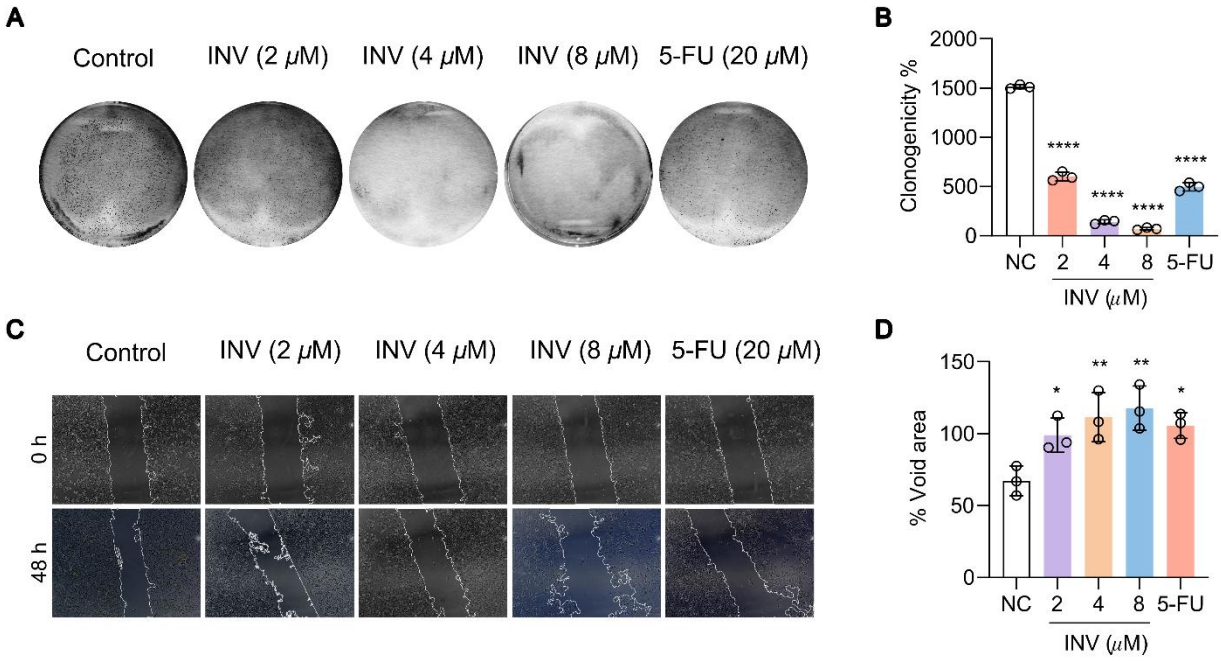


Fig. 2 Clonogenic and antimigratory activity of INV in SW480 cells. (A) and (B) Representative images of colony formation in SW480 cells treated with INV or 5-FU and quantification of clonogenicity (%). (C) and (D) Representative bright-field images of SW480 cell migration at 0 h and 48 h following treatment with INV or 5-FU and quantification of residual void area (%). Data were analysed using one-way ANOVA followed by Dunnett's post hoc multiple comparisons test and are presented as mean ± SD ($n = 3$). *$p < 0.05$, ** $p < 0.01$, and ****$p <$ 0.0001.

Network pharmacology and transcriptomic identification of INV apoptotic targets

To map the predicted target landscape of INV, human protein targets from SwissTarget Prediction were imported into the STRING database (*v*. 12.0) to construct a high-confidence protein-protein interaction (PPI) network (Fig. 3A). Restricting interactions to a stringent minimum confidence threshold of 0.700 resolved a dense, interconnected topology containing multiple high-degree hub proteins, indicating that INV is predicted to drive systemic biological responses through coordinated functional clusters and interconnected signalling hubs, rather than *via* a single isolated target. To identify the specific molecular targets through which INV modulates cell death pathways in CRC, the complete predicted target profile of INV (106 genes) was intersected against the statistically significant transcriptomic profile ($p < 0.05$) of human SW480 cells derived from the GEO dataset GSE345612 (5,403 genes) using Venn diagram analysis (Fig. 3B). This intersection identified a consensus set of five apoptosis-associated target genes shared between the INV target profile and the SW480 disease background: *BAX*, *BCL2*, *CASP3*, *CASP9*, and *CYCS* (Cytochrome c).

To establish the baseline expression context of these targets prior to any drug intervention, a volcano plot was constructed from the differential gene expression matrix of GSE345612 (Fig. 3C), which captures transcriptomic changes in SW480 cells as they transition from 2D monolayer culture to 3D tumour spheroids. In their untreated state, 3D spheroids exhibited upregulation of tumour-promoting markers, *JUN* ($Log_2FC = +1.89$, $p < 0.001$) and *GSK3B*

($Log_2FC = +1.23$, $p < 0.01$), accompanied by moderate downregulation of pro-apoptotic executioner BAX ($Log_2FC = -0.41$), with CASP3, CASP9, and CYCS clustered near baseline levels. BCL2 level was detectable but did not meet the threshold. These findings delineate the pro-survival molecular context within which INV must exerts its apoptotic activity. Mapping the target genes against the Kyoto Encyclopedia of Genes and Genomes (KEGG) database identified 63 statistically significant enriched pathways, notably pathways in cancer (hsa05200; $-\log_{10}(FDR) \approx 12.67$; 23 observed target genes), reflecting the broad oncogenic relevance of the identified targets (Table S6 and Fig. 3D). Additional pathways of mechanistic relevance included MAPK signaling (hsa04010) and NF-κB (hsa04064), which represent upstream regulatory nodes controlling cell fate decisions between survival and apoptosis. In tumour biology, BCL2 promotes cell survival by sequestering pro-apoptotic effectors BAX, and elevated BCL2 expression is conventionally associated with adverse clinical outcomes [28]. However, univariate Cox proportional hazards analysis of TCGA colorectal cancer cohort data) using the GEPIA3 platform revealed that high BCL2 expression was significantly associated with a favourable prognosis, corresponding to a 30.7% reduction in mortality risk (HR = 0.693, CI: 0.503-0.955; $p = 0.0252$) (Fig. 3E). This observation supports the rationale that INV-mediated downregulation of BCL2 in SW480 results in mitochondrial outer membrane permeabilisation (MOMP), leading to apoptosis. The statistical parameters for each target gene are summarised in Table S7. The downstream executioner targets did not reach statistical significance independently: CYCS (HR = 0.773, $p = 0.147$), CASP3 (HR = 0.922, $p = 0.719$), and BAX (HR = 1.049, $p = 0.735$). These findings indicate that while BCL2 acts as a primary prognostic factor, the pleiotropic engagement of the broader apoptotic pathway contributes to its therapeutic benefit.

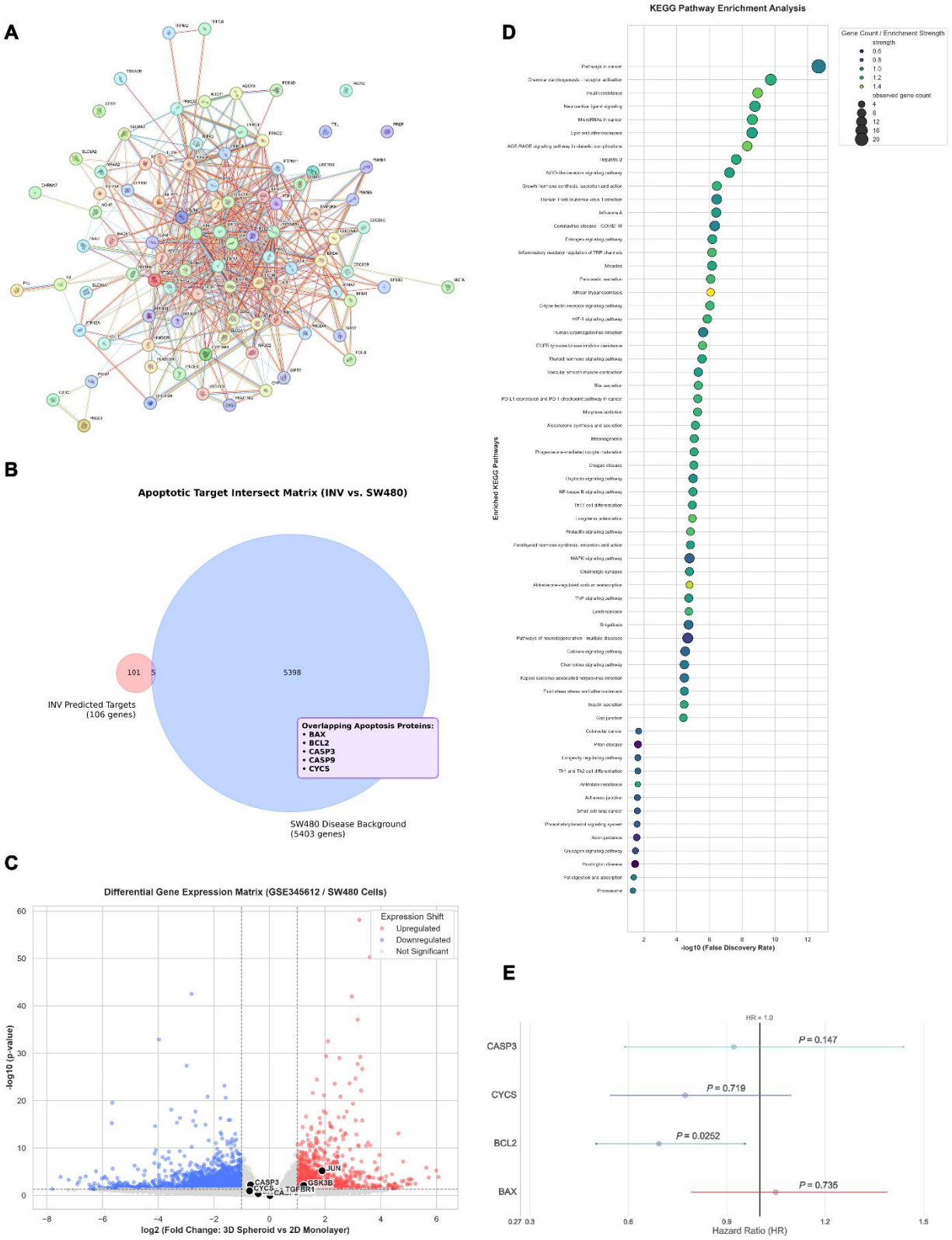

A
B
Apoptotic Target Intersect Matrix (INV vs. SW480)
101
5
5398
INV Predicted Targets
(106 genes)
Overlapping Apoptosis Proteins:
• BAX
• BCL2
• CASP3
• CASP9
• CYCS
SW480 Disease Background
(5403 genes)
C
Differential Gene Expression Matrix (GSE345612 / SW480 Cells)
Expression Shift
Upregulated
Downregulated
Not Significant
-log10 (p-value)
log2 (Fold Change: 3D Spheroid vs 2D Monolayer)
CASP3
CYCS
CA
TGFBR1
GSK3B
JUN
D
KEGG Pathway Enrichment Analysis
Gene Count / Enrichment Strength
strength
observed gene count
Enriched KEGG Pathways
-log10 (False Discovery Rate)
E
HR = 1.0
CASP3
CYCS
BCL2
BAX
P = 0.147
P = 0.719
P = 0.0252
P = 0.735
Hazard Ratio (HR)

Fig. 3 Network pharmacology and transcriptomic profiling of INV apoptotic targets in SW480 Cells. (A) Protein-protein interaction (PPI) network of INV predicted targets. Edges represent interactions filtered at a high-confidence threshold (≥ 0.700). (B) Venn diagram illustrating the intersection between the predicted target profile of INV and the nominally significant transcriptomic background of SW480 cells from the GEO dataset GSE345612**.** (C) Volcano plot of the differential gene expression matrix from GSE345612, depicting transcriptomic shift in SW480 cells transitioning from 2D monolayer culture to 3D tumour spheroids. (D) Bubble plot of statistically significant KEGG pathways enriched within the consensus target network. (E) Forest plot of univariate Cox proportional hazards analysis of apoptotic targets in CRC patients, with horizontal and vertical lines representing 95% confidence intervals and HR 1.0, respectively.

INV exhibits favourable docking interactions with BCL-2 and BAX

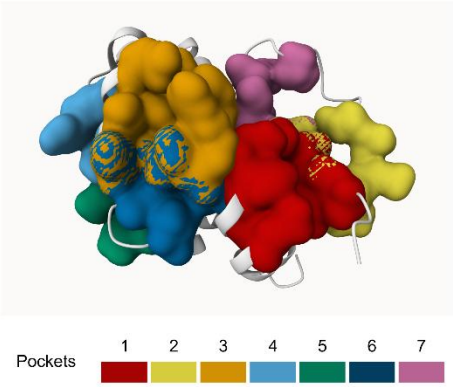
Molecular docking simulations of INV against the primary binding pocket (1) of BCL2 (PDB ID: IG5M) and BAX (PDB ID: 8SPZ) revealed distinct binding modes at each target (Fig. 4A and 4B). Within the BCL2 binding pocket, INV is predominantly mediated by polar interactions with a binding affinity of -7.102 kcal/mol. Specifically, INV formed two conventional hydrogen bonds with ASP A: 196 and TRP A: 195, supplemented by a carbon-hydrogen bond with GLY A: 194. These directional polar contacts are further stabilised by an extensive network of van der Waals contacts with the surrounding pocket residues, including GLN A:190, TYR A:9, THR A:7, GLY A:8, HIS A:186, ILE A:189, GLY A:5, ALA A:4, ARG A:6, and GLY A:193 (Fig. 4C and 4E).

In contrast, the binding affinity within the BAX pocket is governed primarily by hydrophobic insertion and aromatic ring stacking rather than direct hydrogen bonding, with a binding affinity of -7.773 kcal/mol. The complex is anchored by a alkyl and Pi-alkyl contacts involving VAL A:95, ALA A:117, LEU A:113, PHE A:92, PHE A:116, and VAL A:91. Peripheral stabilization within the BAX homodimer groove is maintained via van der Waals forces with LEU A:120, VAL A:83, PRO A:88, VAL A:121, and the dimeric chain residue LEU B:59 (Fig. 4D and 4F; Table 1). Collectively, these interaction profiles demonstrate that while INV engages BLC2 primarily through polar hydrogen-bonding interactions, it adopts a hydrophobic, alkyl/Pi-alkyl-mediated binding mode within the BAX pocket, reflecting the distinct physicochemical environments of the two binding sites.

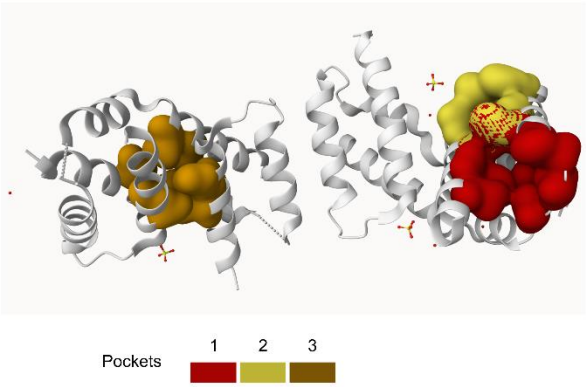
Table 1. Comparative molecular docking interaction profiles of INV within the primary binding pockets of BCL2 and BAX

Target receptor	Binding affinity (kcal/mol)	Interaction type	Interacting residues
BCL2 (IG5M)	-7.102	Conventional hydrogen bonds	ASP A:196 and TRP A:195
		Carbon-hydrogen bond	GLY A:194
		Van der Waals	GLN A:190, TYR A:9, THR A:7, GLY A:8, HIS A:186, ILE A:189, GLY A:5, ALA A:4, ARG A:6, GLY A:193
BAX (8SPZ)	-7.773	Alkyl/Pi-alkyl	VAL A:95, ALA A:117, LEU A:113, PHE A:92, PHE A:116, VAL A:91; LEU B:59
		Van der Waals	LEU A:120, VAL A:83, PRO A:88, VAL A:121

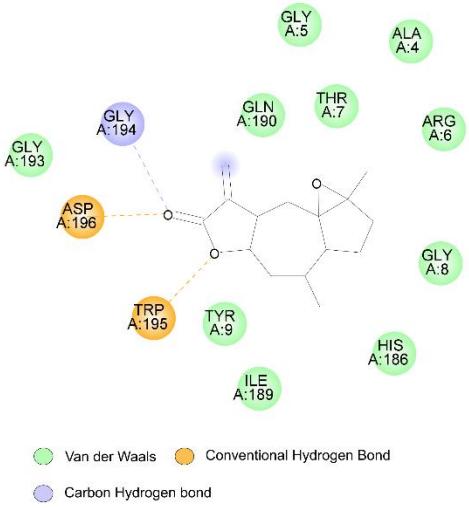
A


Pockets
1
2
3
4
5
6
7

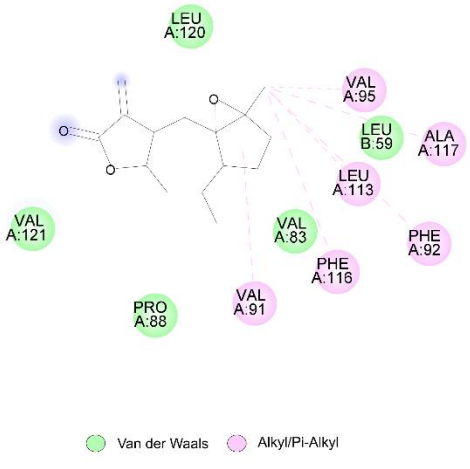
B


Pockets
1
2
3

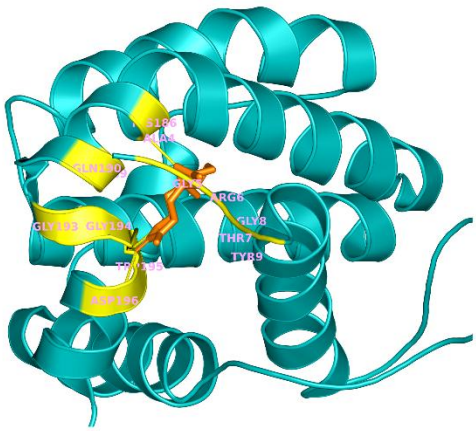
C


GLY A:5
ALA A:4
GLY A:194
GLN A:190
THR A:7
ARG A:6
GLY A:193
ASP A:196
GLY A:8
TRP A:195
TYR A:9
HIS A:186
ILE A:189
Van der Waals
Conventional Hydrogen Bond
Carbon Hydrogen bond

D


LEU A:120
VAL A:95
LEU B:59
ALA A:117
LEU A:113
VAL A:121
VAL A:83
PHE A:92
PHE A:116
PRO A:88
VAL A:91
Van der Waals
Alkyl/Pi-Alkyl

E



F

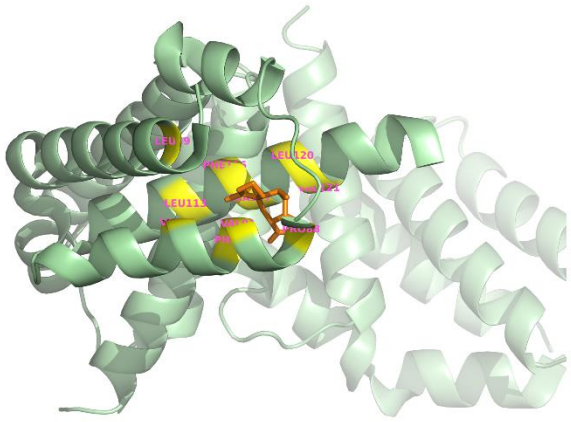


Fig. 4 Molecular docking analysis of INV with BCL2 and BAX. (A and B) Predicted binding pockets of BCL2 and BAX, respectively. (C and D) 2D interaction of INV docked within BCL2 and BAX. (E and F) 3D binding pose of INV within the BCL2 and BAX binding pockets, with interacting residues (yellow), is shown.

INV induces ROS-mediated mitochondrial dysfunction and apoptosis

Scanning electron microscopy (SEM) revealed concentration-dependent apoptotic morphological changes in INV-treated cells, including progressive cellular contraction, membrane blebbing, and the formation of apoptotic bodies (Fig. 5A). Consistent with these findings, DAPI staining demonstrated nuclear morphological alterations, including nuclear irregularity and fragmentation (Fig. 5B).

To investigate the apoptotic mechanism, intracellular redox states and mitochondrial integrity were assessed. DCFH-DA staining revealed a marked accumulation of intracellular ROS in INV-treated cells ($p < 0.01$ at 2 μM; $p < 0.0001$ at 4 and 8 μM) relative to untreated controls (Fig. 5C and F). Dose-dependent reduction in rhodamine-123 staining demonstrated a concentration-dependent reduction in mitochondrial membrane potential ($\Delta\Psi M$; MMP), as evidenced by progressive loss of fluorescence intensity ($p < 0.05$ at 2 μM; $p < 0.0001$ at 4 and 8 μM) relative to untreated controls (Fig. 5D and G). Dual AO/EtBr staining revealed a concentration-dependent shift in cell populations from live towards early and late apoptotic states ($p < 0.0001$ at 4 and 8 μM) following INV treatment (Fig. 5E and H). Collectively, these findings indicate that INV-induced apoptosis in SW480 cells is mechanistically linked to elevated oxidative stress and consequent mitochondrial membrane permeabilisation.

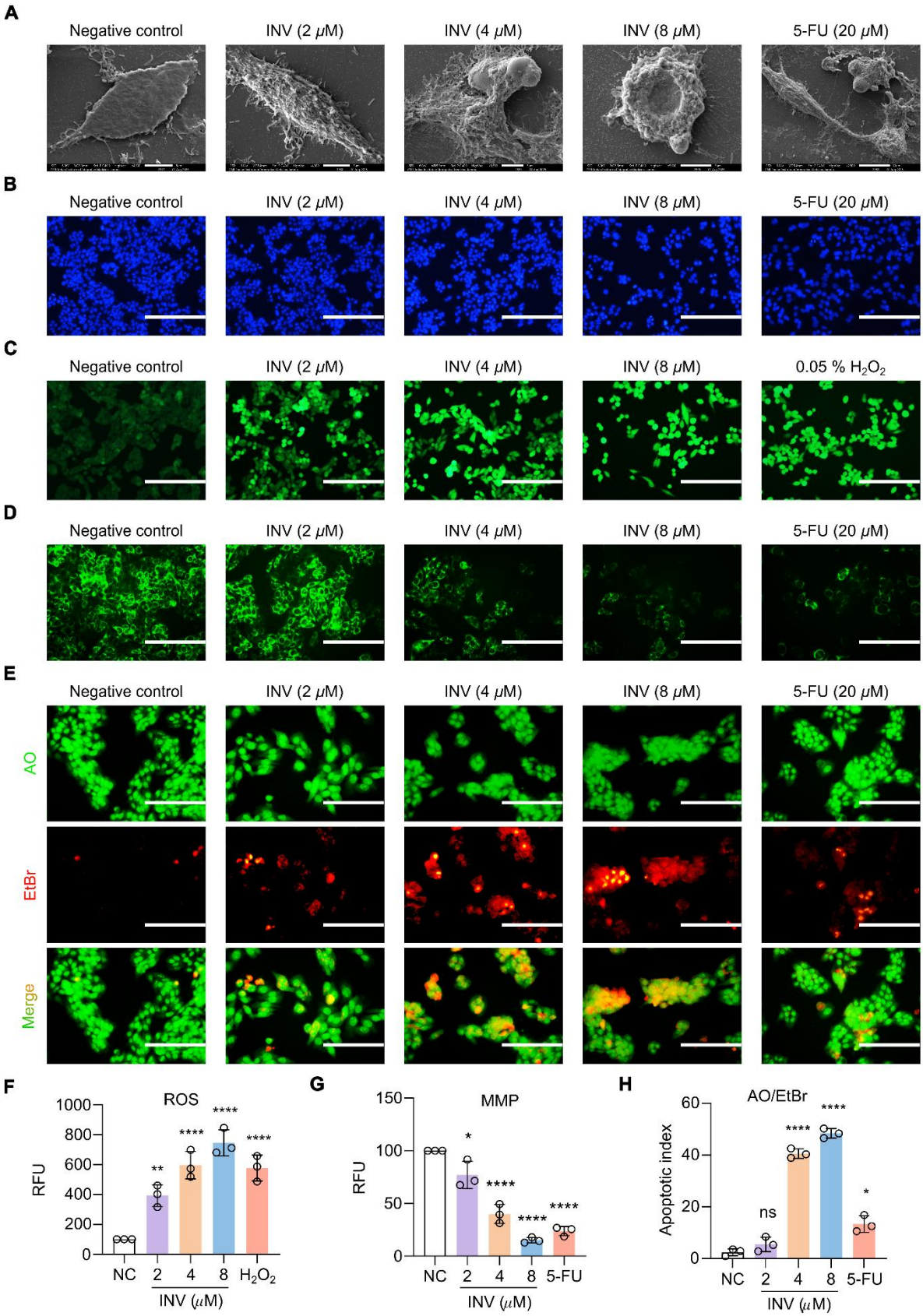

A
Negative control
INV (2 μM)
INV (4 μM)
INV (8 μM)
5-FU (20 μM)
B
Negative control
INV (2 μM)
INV (4 μM)
INV (8 μM)
5-FU (20 μM)
C
Negative control
INV (2 μM)
INV (4 μM)
INV (8 μM)
0.05 % H2O2
D
Negative control
INV (2 μM)
INV (4 μM)
INV (8 μM)
5-FU (20 μM)
E
Negative control
INV (2 μM)
INV (4 μM)
INV (8 μM)
5-FU (20 μM)
AO
EtBr
Merge
F
ROS
RFU
1000
800
600
400
200
0
**
****
****
****
NC
2
4
8
H2O2
INV (μM)
G
MMP
RFU
150
100
50
0
*
****
****
****
NC
2
4
8
5-FU
INV (μM)
H
AO/EtBr
Apoptotic index
60
40
20
0
ns
****
****
*
NC
2
4
8
5-FU
INV (μM)

Fig. 5 INV induces morphological alterations, ROS generation, MMP disruption, and apoptosis in SW480 cells. (A) Representative SEM images showing apoptotic morphological changes**.** (B) Representative fluorescence images demonstrating DAPI-stained nuclear fragmentation. (C and F) Representative fluorescence images demonstrating intracellular ROS accumulation detected using DCFH-DA staining and relative fluorescence intensity (RFU) quantification. (D and G) Representative fluorescence images demonstrating $\Delta\Psi$M loss using rhodamine-123 and RFU quantification. (E and H) Representative fluorescence images demonstrating apoptotic potential of INV in SW480 cells using AO/EtBr staining and quantification of the apoptotic index. 5-FU (20 μM) and H_2O_2 (0.05% *v/v*) were used as the positive control (PC) for all assays and the ROS assay, respectively. Data were analysed using one-way ANOVA, followed by Dunnett's post hoc multiple comparisons test, and are presented as mean ± SD (n = 3). *ns*: non-significant, *$p < 0.05$, **$p < 0.01$, and ****$p < 0.0001$ *vs* untreated control.

To characterise the stage of cell death, Annexin V-FITC/PI dual staining was performed. INV treatment reduced the viable cell population from 86.03% ($p < 0.01$ at 2 μM) to 69.07% ($p < 0.0001$ at 8 μM), accompanied by a progressive increase in both early apoptosis (2.12 to 10.49%; $p < 0.0001$ at 4 and 8 μm) and late apoptosis (11.47 to 20.02%; $p < 0.0001$ at all doses), confirming the apoptotic cell death (Fig. 6A and B). Western blot analysis confirmed concentration-dependent activation of the intrinsic apoptotic pathway (Fig. 6C and D). INV upregulated pro-apoptotic BAX ($p < 0.01$ at 2 μM; $p < 0.0001$ at 4 and 8 μM) and downregulated anti-apoptotic BCL2 ($p < 0.0001$ at all doses). Accumulation of cleaved caspase 3 ($p < 0.001$ at 2 and 4 μM; $p < 0.0001$ at 8 μM) and cleaved PARP ($p < 0.0001$ at all doses), reflecting caspase-3-mediated PARP cleavage and impaired DNA repair capacity. Cytochrome C was elevated ($p < 0.0001$ at all doses) due to membrane permeabilisation.

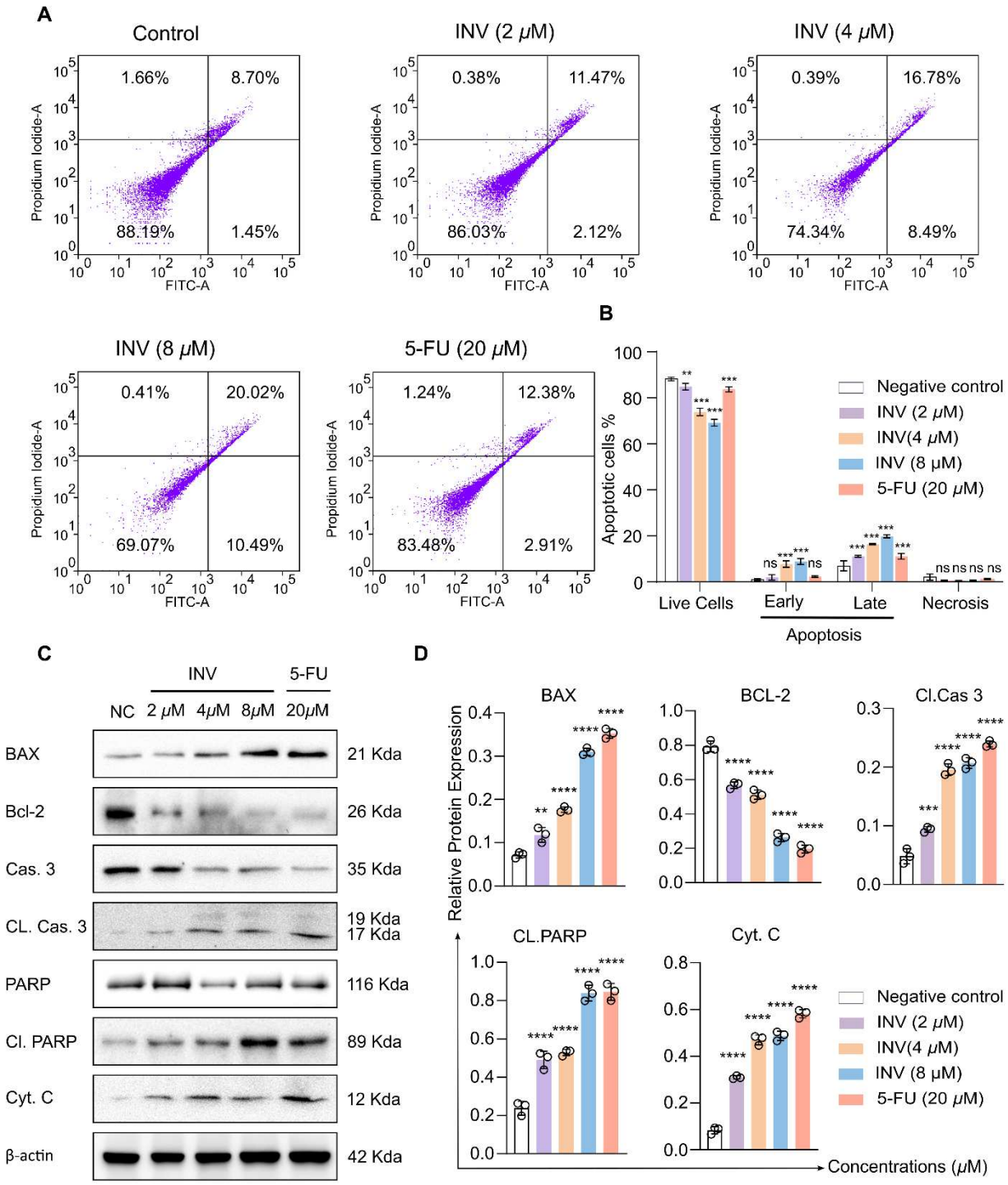


Fig. 6 INV induces early and late apoptosis in SW480 cells. (A and B) Annexin V-FITC/PI flow cytometric scatter plots showing cell populations in various phases following INV treatment and their quantification; (C and D) Western blot analysis and densitometric quantification of intrinsic apoptotic markers. Data were analysed using two-way ANOVA followed by Bonferroni's post hoc multiple comparisons test (B) and one-way ANOVA followed by

Dunnett's post hoc multiple comparisons test (D), and are presented as mean ± SD (n = 3). *ns*: non-significant, *p < 0.05, **p < 0.01, ***p < 0.001, and ****p < 0.0001 *vs* untreated control.

INV induces G1-S phase cell cycle arrest in SW480 cells

INV treatment produced a progressive increase in G1-phase populations from 41.70% (control) to 48.15% (INV - 8 μM), accompanied by an increase in S-phase population (35.99% at 2 μM to 48.06% at 8 μM) and the near-complete depletion of the G2/M population (17.77% at control to 3.79% at 8 μM). In contrast, 5-FU resulted in a marked accumulation of G1-phase cells (56.09%), compared to the S-phase (42.83%), consistent with its established mechanism of S-phase interference and downstream G1 effects (Fig. 7A and B). Western blot analysis demonstrated downregulation of cyclin D1 and CDK-4 (p < 0.0001 at 8 μM), key regulators of the G1/S checkpoint (Fig. 7C and D).

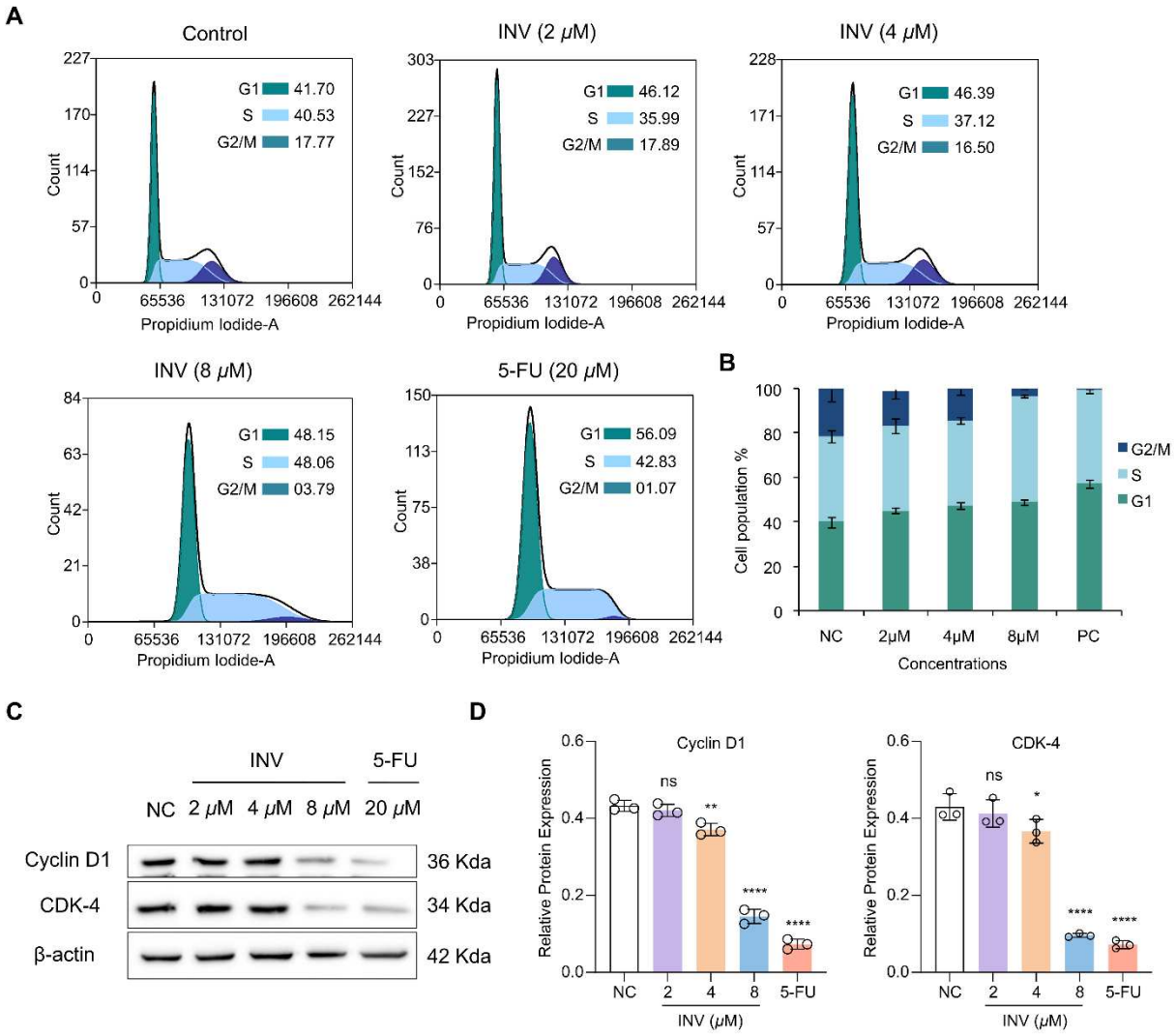


Fig. 7 INV induces G1-S phase cell cycle arrest in SW480 cells. (A and B) Flow cytometric histograms showing the cell cycle distribution of SW480 cells following INV treatment, with quantification. (C and D) Western blot analysis

and densitometric quantification of cyclin D1 and CDK-4. β-actin as the loading control. Data were analysed using one-way ANOVA followed by Dunnett's post hoc multiple comparisons test, and are presented as mean ± SD (n = 3). *ns*: non-significant, *$p < 0.05$, **$p < 0.01$, and ****$p <$ 0.0001 *vs* untreated control.

INV suppresses SW480 xenograft tumour growth in vivo

Oral administration of INV promoted 78.26% (40 MPK) and 98.7% (80 MPK) tumour growth inhibition, as evident from tumour volume reduction ($p < 0.0001$ at both doses), tumour weight ($p < 0.05$ at 40 MPK and $p < 0.01$ at 80 MPK), and gross images (Fig. 8B-D, F and H). Body weight remained stable across all groups with no significant between-group differences in the body weight/tumor weight ratio, indicating that INV was well tolerated at both doses (Fig. 8E and 8G).

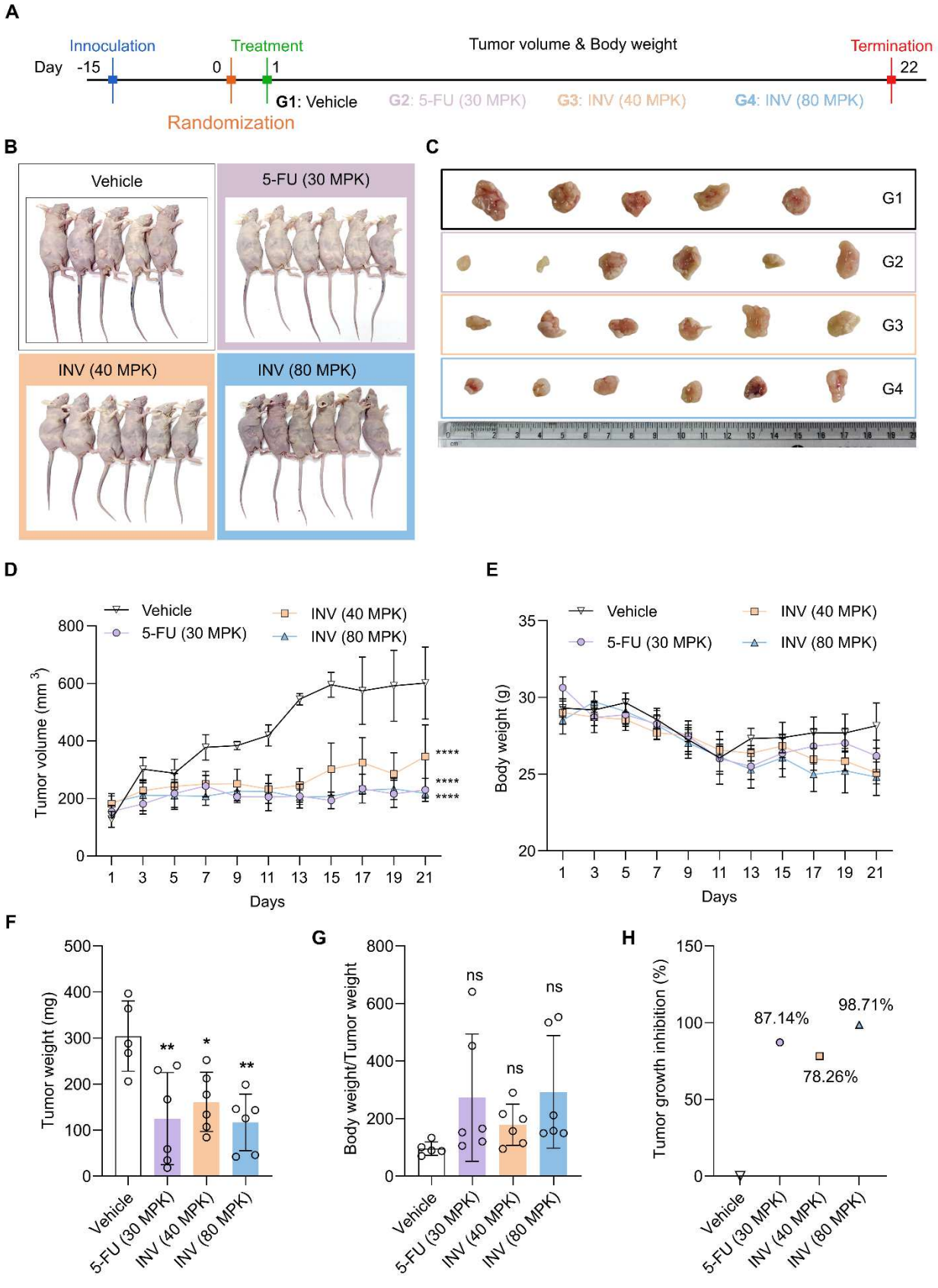

A
Innoculation
Treatment
Tumor volume & Body weight
Termination
Day -15
0
1
22
G1: Vehicle
G2: 5-FU (30 MPK)
G3: INV (40 MPK)
G4: INV (80 MPK)
Randomization
B
Vehicle
5-FU (30 MPK)
INV (40 MPK)
INV (80 MPK)
C
G1
G2
G3
G4
D
Vehicle
5-FU (30 MPK)
INV (40 MPK)
INV (80 MPK)
Tumor volume (mm 3)
Days
****
****
****
E
Vehicle
5-FU (30 MPK)
INV (40 MPK)
INV (80 MPK)
Body weight (g)
Days
F
Tumor weight (mg)
**
*
**
Vehicle
5-FU (30 MPK)
INV (40 MPK)
INV (80 MPK)
G
Body weight/Tumor weight
ns
ns
ns
Vehicle
5-FU (30 MPK)
INV (40 MPK)
INV (80 MPK)
H
Tumor growth inhibition (%)
87.14%
98.71%
78.26%
Vehicle
5-FU (30 MPK)
INV (40 MPK)
INV (80 MPK)

Fig. 8 Oral administration of INV suppresses SW480 xenograft tumour growth. (A) Schematic study timeline. (B) Gross photographs of mice with tumours. (C) Excised tumours from all groups. (D) Tumour volume (mm^3). (E) Body weight (g) over the treatment period. (F) Excised tumour weight (mg). (G) Terminal body weight/tumour weight ratio. (H) Tumour growth inhibition (TGI, %). Data were analysed using one-way ANOVA followed by Dunnett's post hoc multiple comparisons test and are presented as mean ± SD (n = 5 for vehicle control; n = 6 for all other groups). *ns*: non-significant, *$p < 0.05$, **$p < 0.01$, and ****$p < 0.0001$ vs vehicle control.

Preliminary safety assessment of INV

A single oral dose of INV at 300 MPK, administered in accordance with OECD 423, produced no treatment-related mortality or clinical signs of toxicity. A confirmatory cohort of 3 animals at the same dose (Annexure 2C) confirmed these findings, with no reduction in body weight. Studies were continued with the next higher dose (2000 MPK), using an additional cohort of 3 animals (Annexure 2D), which revealed similar findings, classifying INV as GHS category 5 or unclassified and indicating an LD_{50} cutoff > 5000 MPK (Fig. 9A and B).

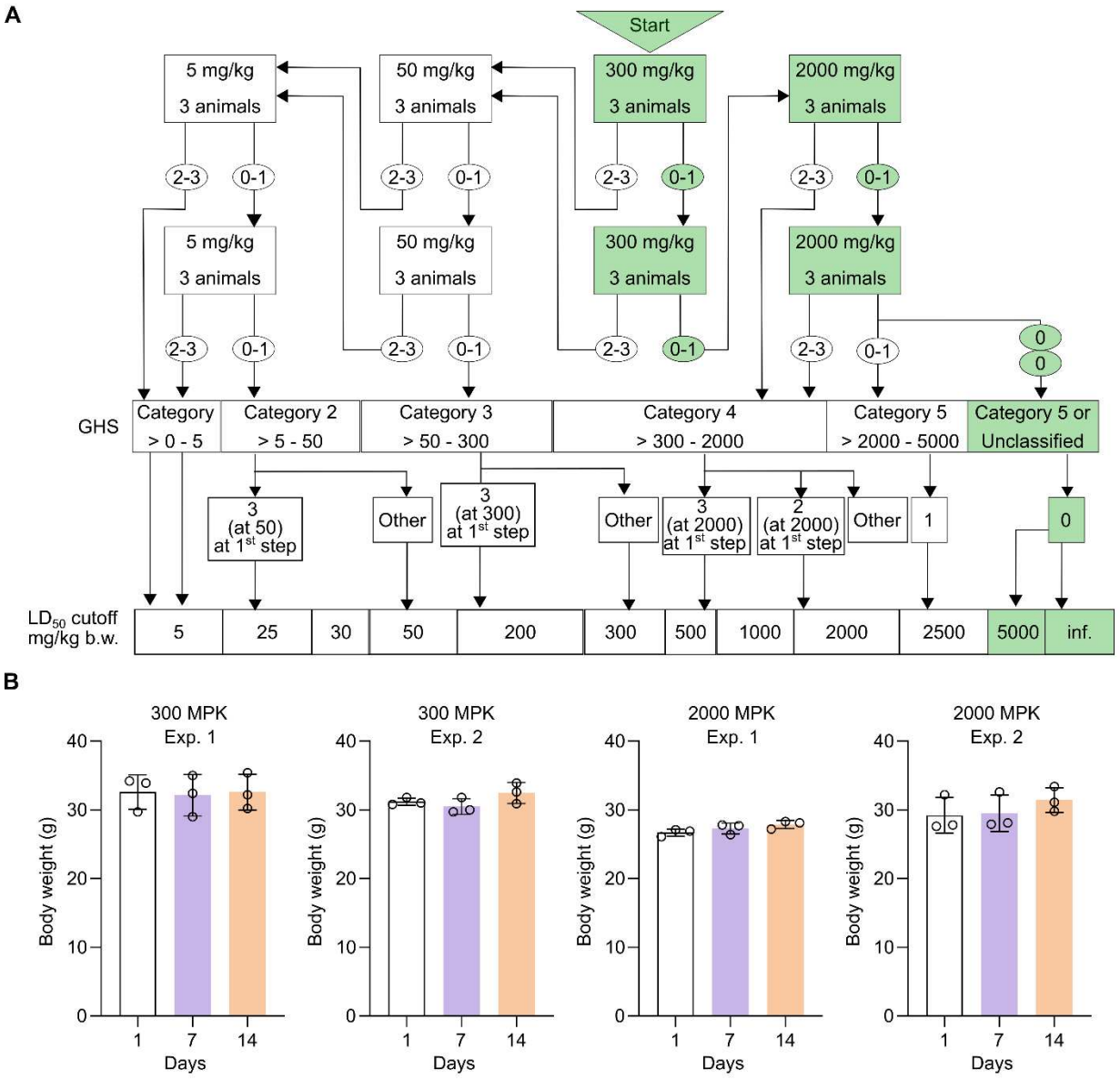


Fig. 9 Acute oral toxicity assessment of INV in Swiss albino mice. (A) Schematic of test procedure, with starting doses of 300 to 2000 MPK as described in OECD 423 Annexure 2C and 2D; highlighted (green) boxes indicate the path taken. (B) Body weights (g) of mice (n = 3 per experiment) measured at weekly intervals at two doses in both experiments.

Discussion

CRC represents the third most commonly diagnosed cancer globally, characterised by high recurrence rates, tumour heterogeneity, therapeutic resistance, and dose-limiting toxicity associated with conventional chemotherapies. These clinical challenges underscore the need for novel, naturally derived bioactive compounds with favourable safety profiles [29].

In the present study, INV inhibited SW480 CRC cell proliferation (IC_{50} 4.65 μM) and promoted significant *in* vivo tumour growth inhibition (78.26% and 98.71% at 40 and 80 MPK, respectively). The integrated computational framework demonstrated a hierarchical mechanism of action for INV within the SW480 3D tumour spheroid environment. In the untreated state, the 3D spheroid architecture activates upstream NF-κB and MAPK signalling cascades, thereby promoting transcriptional upregulation of the anti-apoptotic BCL2 [30]. This anti-apoptotic protection allows BCL2 to sequester pro-apoptotic effectors, effectively neutralising the intrinsic apoptotic pathway. INV downregulated BCL2 expression, shifting the BAX/BCL2 ratio favouring apoptosis. This depletion of the BCL2 pool liberates BAX from sequestration, allowing it to self-assemble into functional homodimers and initiate MOMP [31, 32]. MOMP promotes cytochrome c (CYCS) release from the mitochondrial intermembrane space, which subsequently triggers downstream activation of the caspase cascade (CASP9 and CASP3). Collectively, these findings indicate that INV overcomes the pro-survival signalling in SW480 cells, thereby activating the intrinsic mitochondrial apoptotic pathway. Notably, BCL2 emerged as a statistically significant independent prognostic determinant in the CRC cohort (HR = 0.693; 95% CI: 0.503- 0.955; z = -2.239; p = 0.0252), indicating that elevated BCL2 expression is associated with a 30.7% reduction in mortality risk, providing a favourable prognostic association of BCL2 in CRC, as reported previously.

In our experimental model, INV downregulated BCL2 expression in SW480 cells. While untreated 3D tumour architectures suppress the cell death machinery to survive, they remain dependent on residual BCL2 levels to prevent apoptotic collapse [33]. By depleting this residual anti-apoptotic buffer, INV effectively liberates BAX, initiating MOMP and driving caspase-mediated apoptosis. Collectively, the system-level analysis indicates that INV may act as a multi-target modulator, suppressing upstream pro-survival signaling cascades while simultaneously engaging the intrinsic apoptotic program. Molecular docking simulations further demonstrated favourable binding interactions of INV within the active binding pockets of both anti-apoptotic BCL2 and pro-apoptotic BAX.

INV exhibited concentration-dependent cytotoxicity and inhibition of cell migration in SW480 cells, shifting the cellular survival balance by upregulating BAX, cleaved caspase 3, cleaved PARP, and cytochrome C, while downregulating BCL2. Mechanistically, INV elevated intracellular ROS levels and disrupted mitochondrial membrane potential ($\Delta\Psi M$), triggering cytochrome c release from the mitochondrial intermembrane space into the cytoplasm. The release initiated the caspase execution cascade, marked by activation of cleaved caspase 3 and PARP cleavage, thereby impairing the cell's capacity to repair DNA [34]. Flow cytometric analysis confirmed these findings with a concentration-dependent increase in early and late apoptotic populations [35]. These biochemical changes resulted in characteristic morphological apoptotic alterations, as confirmed by SEM [36]. In addition, INV disrupted

cell cycle progression with concentration-dependent G1-phase accumulation, consistent with downregulation of cyclin D1 and CDK-4, key regulators of the G1/S checkpoint required for S-phase entry [37, 38].

Consistent with *in vitro* findings, *in vivo* SW480 xenograft studies corroborated these observations. Oral administration of INV produced dose-dependent anti-tumour effects, with 78.26% and 98.7% inhibition of tumour growth at 40 and 80 MPK, respectively, without significant body weight loss. Preliminary safety evaluation showed no mortality or body weight reduction at doses up to 2000 mg/kg, indicating tolerability under the experimental conditions.

Conclusion

Overall, to the best of our knowledge, this study provides the first evidence of the pro-apoptotic and *in vivo* anti-tumour activities of INV in a CRC model. INV exerted potent anticancer effects against SW480 cells by inhibiting cell proliferation, disrupting cell cycle progression, elevating oxidative stress, impairing mitochondrial function, and activating the intrinsic apoptotic pathway. The observed *in vivo* inhibition of tumour growth further supports INV as a promising lead. Network pharmacology, transcriptomic integration, KEGG enrichment analysis, and molecular docking identified apoptosis-associated pathways and predicted binding interactions involving BAX and BCL2. The integrated in silico, in vitro, and in vivo findings establish a foundation for investigating the molecular mechanism and therapeutic potential of INV in CRC.

Author contribution Bikram Singh: Formal analysis, Investigation, Visualisation, Writing - original draft. Shivani Rana: Formal analysis, Investigation. Komal: Isolation. Zabeer Ahmed: Resources, Supervision. Yedukondalu Nalli: Investigation. Boobalan Gopu: Conceptualisation, Formal analysis, Funding acquisition, resources, Supervision, Visualisation, Writing - original draft and reviewing.

Funding BG acknowledges funding from DST-ANRF, India, under grant number (EEQ/2023/001123), and CSIR-India, ULIP project (MLP002622) for this work.

Data availability Any additional details will be made available upon reasonable request to the corresponding author.

Declaration of competing interests All authors declare that they have no known financial or personal conflicts of interest related to this study.

Acknowledgements The authors thank Zabeer Ahmed, Director, CSIR-Indian Institute of Integrative Medicine (CSIR-IIIM), Jammu, India, for providing technical guidance, facilities, and resources. Yedukondalu Nalli acknowledges Manu Khajuria for plant materials.

References

1. Fadlallah H, El Masri J, Fakhereddine H, Youssef J, Chemaly C, Doughan S et al (2024) Colorectal cancer: Recent advances in management and treatment. World J Clin Oncol 15(9): 1136. https://doi.org/10.5306/wjco.v15.i9.1136
2. Sung H, Filho AM, Laversanne M, Ferlay J, Siegel RL, Soerjomataram I et al (2026) Global cancer statistics 2024: GLOBOCAN estimates of incidence and mortality worldwide for 34 cancers in 186 countries. CA Cancer J Clin 76(4): e70090. https://doi.org/10.3322/caac.70090
3. Shin A, Jung K-W, Jeong S-Y (2023) Right then, wrong now: early-onset colorectal cancer in Korea. Cancer Res Treat 55(3): 1058-1060. https://doi.org/10.4143/crt.2022.1612
4. Tirendi S, Marengo B, Domenicotti C, Bassi AM, Almonti V, Vernazza S (2023) Colorectal cancer and therapy response: a focus on the main mechanisms involved. Front Oncol 131208140. https://doi.org/10.3389/fonc.2023.1208140
5. Zhang S, Won Y-K, Ong C-N, Shen H-MJCMC-A-CA (2005) Anti-cancer potential of sesquiterpene lactones: bioactivity and molecular mechanisms. Curr Med Chem Anticancer Agents 5(3): 239-249. https://doi.org/10.2174/1568011053765976
6. Singh B, Thappa C, Komal, Laasya Priya P, Begum S, Nalli Y et al (2026) Two new dibenzyl-gamma-butyrolactone lignans with cytotoxic activity from Himalaiella heteromalla, an Indian Himalayan plant. Nat Prod Res 40(13): 3910-3917. https://doi.org/10.1080/14786419.2025.2491122
7. Singh B, Thappa C, Nalli Y, Gopu B (2025) Cytotoxic 6,12-guaianolides from Himalaiella heteromalla (D.Don) Raab-Straube: mechanistic investigations in pancreatic cancer cells. Nat Prod Res 1-8. https://doi.org/10.1080/14786419.2025.2588793
8. Sharma M, Kumar A, Nalli Y, Khajuria M, Singh K (2026) Antimicrobial assessment and scanning electron microscopy analysis of sesquiterpene lactones isolated from the leaves of Inula racemosa Hook. f. Arch Microbiol 208(7): 354. https://doi.org/10.1007/s00203-026-04915-5
9. Komal, Thappa C, Sharma K, Begum S, Sultan F, Khajuria M et al (2025) Inulevs-A, a new sesquiterpene lactone from the leaves of Inula racemosa Hook. f.". Nat Prod Res 1-8. https://doi.org/10.1080/14786419.2025.2569805
10. Lee J, Min B, Lee S, Na M, Kwon B, Lee C et al (2002) Cytotoxic sesquiterpene lactones from Carpesium abrotanoides. Planta Med 68(8): 745-7. https://doi.org/10.1055/s-2002-33789
11. Ko YE, Oh SR, Song HH, Ryu HW, Ly SY, Kim JW (2015) The effect of 4alpha,5alpha-epoxy-10alpha,14-dihydro-inuviscolide, a novel immunosuppressant isolated from Carpesium abrotanoides, on the cytokine profile in vitro and in vivo. Int Immunopharmacol 25(1): 121-9. https://doi.org/10.1016/j.intimp.2015.01.002
12. Momen-Roknabadi N, Gohari AR, Monsef-Esfehani HR, Attar F, Hajiaghaee R, Saeidnia S et al (2008) Antifungal and antibacterial activities of Pentanema divaricatum and its active constituent. Z Naturforsch C J Biosci 63(9-10): 649-52. https://doi.org/10.1515/znc-2008-9-1006
13. Franken NA, Rodermond HM, Stap J, Haveman J, van Bree C (2006) Clonogenic assay of cells in vitro. Nat Protoc 1(5): 2315-9. https://doi.org/10.1038/nprot.2006.339
14. Liang CC, Park AY, Guan JL (2007) In vitro scratch assay: a convenient and inexpensive method for analysis of cell migration in vitro. Nat Protoc 2(2): 329-33. https://doi.org/10.1038/nprot.2007.30

15. Daina A, Michielin O, Zoete V (2019) SwissTargetPrediction: updated data and new features for efficient prediction of protein targets of small molecules. Nucleic Acids Res 47(W1): W357-W364. https://doi.org/10.1093/nar/gkz382
16. Szklarczyk D, Kirsch R, Koutrouli M, Nastou K, Mehryary F, Hachilif R et al (2023) The STRING database in 2023: protein-protein association networks and functional enrichment analyses for any sequenced genome of interest. Nucleic Acids Res 51(D1): D638-D646. https://doi.org/10.1093/nar/gkac1000
17. Love MI, Huber W, Anders S (2014) Moderated estimation of fold change and dispersion for RNA-seq data with DESeq2. Genome Biol 15(12): 550. https://doi.org/10.1186/s13059-014-0550-8
18. Heberle H, Meirelles GV, da Silva FR, Telles GP, Minghim R (2015) InteractiVenn: a web-based tool for the analysis of sets through Venn diagrams. BMC Bioinformatics 16(1): 169. https://doi.org/10.1186/s12859-015-0611-3
19. Al-Duais MA, El Rabey HA, Mohammed GM, Al-Awthan YS, Althiyabi AS, Attia ES et al (2025) The anticancer activity of fucoidan coated selenium nanoparticles and curcumin nanoparticles against colorectal cancer lines. Sci Rep 15(1): 287. https://doi.org/10.1038/s41598-024-82687-y
20. Liu Z, Tan X, Peng L, Gao W, Zeng P (2024) Hederagenin Induces Apoptosis of Human Hepatoma HepG2 Cells via the Mitochondrial Pathway. Comb Chem High Throughput Screen 27(10): 1495-1503. https://doi.org/10.2174/0113862073254353230925074944
21. Ramadan FHJ, Koszegi B, Vantus VB, Fekete K, Kiss GN, Rizsanyi B et al (2024) Comparison of Mitochondrial and Antineoplastic Effects of Amiodarone and Desethylamiodarone in MDA-MB-231 Cancer Line. Int J Mol Sci 25(18). https://doi.org/10.3390/ijms25189781
22. Mohamed HRH, Borai ME, Mosaad S, Osman AA, Elsewedy AH, Zaki HM et al (2026) Bioactive glass nanoparticles induce intrinsic p53-dependent apoptosis and promote genomic instability via ROS overproduction and mitochondrial depolarization in triple-negative breast cancer cells. Sci Rep 16(1): 809. https://doi.org/10.1038/s41598-025-32827-9
23. Turhal G, Demirkan B, Baslilar IN, Yuncu NS, Baytas SN, Demiroglu-Zergeroglu A (2024) Preliminary evaluation of antiproliferative and apoptotic activities of novel indolin-2-one derivatives. Drug Dev Res 85(5): e22229. https://doi.org/10.1002/ddr.22229
24. Ha SG, Park JH, Kim MY, Lee SV (2025) Brief guide to western blot assays. Mol Cells 48(12): 100297. https://doi.org/10.1016/j.mocell.2025.100297
25. Wang H, Joseph JA (1999) Quantifying cellular oxidative stress by dichlorofluorescein assay using microplate reader. Free Radic Biol Med 27(5-6): 612-6. https://doi.org/10.1016/s0891-5849(99)00107-0
26. Council NR, Guide for the Care and Use of Laboratory Animals. 2011: Washington (DC). https://doi.org/10.17226/12910.
27. Chen C, Zhu D, Zhang H, Han C, Xue G, Zhu T et al (2018) YAP-dependent ubiquitination and degradation of beta-catenin mediates inhibition of Wnt signalling induced by Physalin F in colorectal cancer. Cell Death Dis 9(6): 591. https://doi.org/10.1038/s41419-018-0645-3
28. Kelly PN, Strasser A (2011) The role of Bcl-2 and its pro-survival relatives in tumourigenesis and cancer therapy. Cell Death Differ 18(9): 1414-24. https://doi.org/10.1038/cdd.2011.17

29. Kee JX, Yau JNN, Kumar Muthuramalingam RP, Wang X, Chng WH, Lopez-Sanchez A et al (2025) Colorectal cancer at the crossroads: the good, the bad, and the future of platinum-based drugs. Chem Rev 125(21): 10248-10341. https://doi.org/10.1021/acs.chemrev.5c00041
30. Chan YH, Lee YC, Hung CY, Yang PJ, Lai PC, Feng SW (2021) Three-dimensional Spheroid Culture Enhances Multipotent Differentiation and Stemness Capacities of Human Dental Pulp-derived Mesenchymal Stem Cells by Modulating MAPK and NF-kB Signaling Pathways. Stem Cell Rev Rep 17(5): 1810-1826. https://doi.org/10.1007/s12015-021-10172-4
31. Kale J, Osterlund EJ, Andrews DW (2018) BCL-2 family proteins: changing partners in the dance towards death. Cell Death Differ 25(1): 65-80. https://doi.org/10.1038/cdd.2017.186
32. Pena-Blanco A, Garcia-Saez AJ (2018) Bax, Bak and beyond - mitochondrial performance in apoptosis. FEBS J 285(3): 416-431. https://doi.org/10.1111/febs.14186
33. Youle RJ, Strasser A (2008) The BCL-2 protein family: opposing activities that mediate cell death. Nat Rev Mol Cell Biol 9(1): 47-59. https://doi.org/10.1038/nrm2308
34. Lu X, Li C, Wang Y-K, Jiang K, Gai X-D (2014) Sorbitol induces apoptosis of human colorectal cancer cells via p38 MAPK signal transduction. Oncol Lett 7(6): 1992-1996. https://doi.org/10.3892/ol.2014.1994
35. Yang D, He L, Ma S, Li S, Zhang Y, Hu C et al (2023) Pharmacological targeting of Bcl-2 induces caspase 3-mediated cleavage of HDAC6 and regulates the autophagy process in colorectal cancer. Int J Mol Sci 24(7): 6662. https://doi.org/10.3390/ijms24076662
36. Elmore S (2007) Apoptosis: a review of programmed cell death. Toxicol pathol 35(4): 495-516. https://doi.org/10.1080/01926230701320337.
37. Meng L-h, Zhang H, Hayward L, Takemura H, Shao R-G, Pommier Y (2004) Tetrandrine induces early G1 arrest in human colon carcinoma cells by down-regulating the activity and inducing the degradation of G1-S–specific cyclin-dependent kinases and by inducing p53 and p21Cip1. Cancer Res 64(24): 9086-9092. https://doi.org/10.1158/0008-5472.CAN-04-0313
38. Lee S-K, Kim H-N, Kang Y-R, Lee CW, Kim H-M, Han DC et al (2008) Obovatol inhibits colorectal cancer growth by inhibiting tumor cell proliferation and inducing apoptosis. Bioorg Med Chem 16(18): 8397-8402. https://doi.org/10.1016/j.bmc.2008.08.033

Supplementary Files

This is a list of supplementary files associated with this preprint. Click to download.

- ESM3SupplementaryTablesS1S7.xlsx
- ESM2SupplementaryfigureS2.pdf
- ESM1SupplementaryfigureS1.pdf